TaS₂, TaSe₂, and Their Heterogeneous Films as Catalysts for the Hydrogen Evolution Reaction

Leyla Najafi,[‡] Sebastiano Bellani,[‡] Reinier Oropesa-Nuñez, Beatriz Martín-García, Mirko Prato, Lea Pasquale, Jaya-Kumar Panda, Petr Marvan, Zdeněk Sofer, and Francesco Bonaccorso*

Cite This: *ACS Catal.* 2020, 10, 3313−3325

Read Online

ACCESS | Metrics & More | Article Recommendations | Supporting Information

ABSTRACT: Metallic two-dimensional transition-metal dichalcogenides (TMDs) of the group 5 metals are emerging as catalysts for an efficient hydrogen evolution reaction (HER). The HER activity of the group 5 TMDs originates from the unsaturated chalcogen edges and the highly active surface basal planes, whereas the HER activity of the widely studied group 6 TMDs originates solely from the chalcogen- or metal-unsaturated edges. However, the batch production of such nanomaterials and their scalable processing into high-performance electrocatalysts is still challenging. Herein, we report the liquid-phase exfoliation of the 2H-TaS₂ crystals by using 2-propanol to produce single/few-layer (1H/2H) flakes, which are afterward deposited as catalytic films. A thermal treatment-aided

Texturised heterogeneous TaS₂:TaSe₂ films for HER

texturization of the catalytic films is used to increase their porosity, promoting the ion access to the basal planes of the flakes, as well as the number of catalytic edges of the flakes. The hybridization of the H-TaS₂ flakes and H-TaSe₂ flakes tunes the Gibbs free energy of the adsorbed atomic hydrogen onto the H-TaS₂ basal planes to the optimal thermo-neutral value. In 0.5 M H₂SO₄, the heterogeneous catalysts exhibit a low overpotential (versus RHE, reversible hydrogen electrode) at the cathodic current of 10 mA cm⁻² (η_{10}) of 120 mV and high mass activity of 314 A g⁻¹ at an overpotential of 200 mV. In 1 M KOH, they show a η_{10} of 230 mV and a mass activity of 220 A g⁻¹ at an overpotential of 300 mV. Our results provide new insight into the usage of the metallic group 5 TMDs for the HER through scalable material preparation and electrode processing.

KEYWORDS: transition-metal dichalcogenides (TMDs), tantalum disulfide (TaS₂), tantalum diselenide (TaSe₂), hydrogen evolution reaction (HER), heterogeneous catalysts
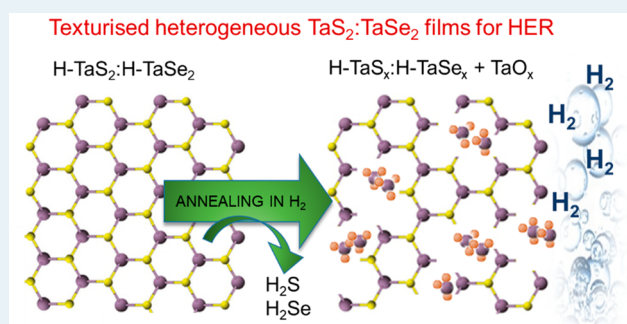
1. INTRODUCTION

Molecular hydrogen (H₂) has been touted as an ideal energy carrier with high energy density (between 120 and 140 MJ kg⁻¹).[1] In fact, it can be generated by electrochemical water splitting powered by renewable resources,[2] and its utilization, giving water as a byproduct, is sustainable and environmentally friendly.[3] To spread the use of H₂ as energy fuel, i.e., to make feasible the so-called "Hydrogen economy" model,[4,5] it is crucial to develop efficient electrocatalysts. The latter have to promote the hydrogen evolution reaction (HER) (i.e., 4H₃O⁺ + 4e⁻ → 4H₂O + 2H₂ in acidic media; 4H₂O + 4e⁻ → 2H₂ + 4OH⁻ in alkaline media)[6] accelerating its kinetics.[7] The most effective electrocatalysts for the HER are expensive and scarce Pt-group elements.[8−10] Therefore, the upscaling of electrochemical technology for HER is currently inspiring the search for viable catalyst alternatives,[11−14] including low Pt-content alloys[15−17] or low-cost transition-metal-based alloys, compounds, and heterostructures.[11−13,18]

In this context, the transition-metal dichalcogenides (TMDs), made of covalently bonded C−M−C units (M = transition metal; C = chalcogen, i.e., S, Se, Te),[19,20] have

attracted strong interest for the HER.[21−24] Theoretical[25−27] and experimental[28−31] investigations have shown that the HER active sites of the natural semiconducting phase (2H) of molybdenum (Mo)- and tungsten (W)-based TMDs are chalcogen-unsaturated edges, since they have a close to zero Gibbs free energy for the atomic H adsorption (ΔG_H) in acidic condition. To fully exploit such high per site HER activity, the controllable synthesis of nanostructured TMDs[27,29,32−34] has been pursued to maximize the number of the catalytically active edges.[35−37] The designed nanostructured TMDs have shown the possibility to reach overpotential at a cathodic current density of 10 mA cm⁻² (η_{10}) inferior to 0.1 V, approaching that of noble-metal-based electrocatalysts.[35−37] However, the complex material nanostructuring unavoidably tackles cost and scalability concerns, pointing out the need of

alternative strategies. Recently, the metallic 2H-TMDs based on group 5 metals (i.e., tantalum (Ta), niobium (Nb), and vanadium(V)) have raised paramount appeal for the HER because of their intrinsic basal plane activity (especially for the sulfides)[38−44] that is beyond that of either metal or chalcogen edges.[41−44] The latter statement has been confirmed by density functional theory (DFT) calculations, whose outcomes are summarized in Figure 1.[25,39,41,42,45] Clearly, the catalytic
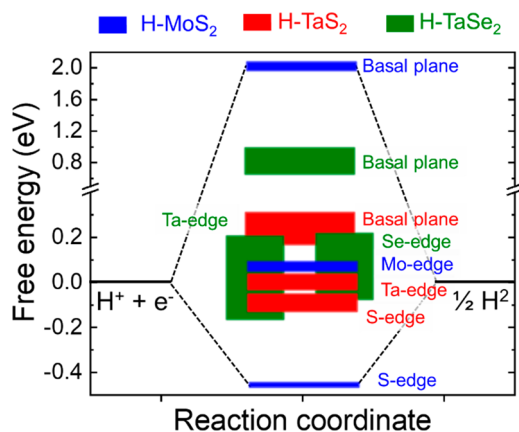

Figure 1. Standard ΔG_H ranges of different sites of semiconducting H−MoS$_2$, metallic H-TaS$_2$ and metallic H-TaSe$_2$. Rectangles are used to indicate the data range that has been extrapolated from the literature for ΔG_H (refs 25, 39, 41, 42, and 45).

properties of their basal planes could make these materials compatible with scalable existing electrode designs. To date, 2H-TaS$_2$ nanoplatelets synthesized by chemical vapor deposition (CVD) have displayed record-high surface HER activity (e.g., η_{10} < 60 mV with a loading of the catalyst <60 μg cm^{-2}) among all of the reported TMDs.[40] However, such Pt-competing HER activity has been achieved after a peculiar electrochemical treatment, namely, thousands of cyclic voltammetry (CV) scans. This peculiar behavior is still under debate, and it has been mainly attributed to morphological changes of the 2H-TaS$_2$ nanoplatelets.[40] More in detail, theoretical/experimental results on CVD-synthesized 2H-TaS$_2$ nanoplatelets supported a cycling-induced self-optimizing morphology evolution from thick to thin platelets without any noticeable changes neither in the crystal structure nor in the chemical composition of the materials.[40] Such morphological changes have been associated with a fastening of electron transport with shortening of the interlayer electron-transfer pathways in thin samples, as well as to an improved accessibility of aqueous proton (H$_3$O$^+$) to the catalytic sites.[40] However, such self-optimizing fragmentation could cause degradation of the electrode in absence of polymeric binding agents (e.g., perfluorosulfonic acid, Nafion).[46] In particular, the catalyst fracturing could affect the adhesion of the catalytic film to the electrode, and the maximum HER activity could be progressively degraded after reaching the optimal electrode morphology.[46] Furthermore, other works claimed that the surface oxides formed on the air-exposed TaS$_2$ surface are peeled off by H$_2$ bubbles as the HER proceeds. Therefore, the real HER activity of the 2H-TaS$_2$ is exhibited subsequently.[41] Though, clear experimental evidence of this effect and the absence of surface oxidation are still lacking, especially for electrodes using mass loading relevant for real electrolyzers. Accordingly, further understanding of the processing and use

of the metallic group 5 TMDs for the HER are required for their practical prototype validation.

In this work, we produce single/few-layer H-TaS$_2$ flakes (i.e., 1H-TaS$_2$ monolayers and 2H-TaS$_2$ flakes) by an eco-friendly liquid-phase exfoliation (LPE) of the material crystals synthesized through direct synthesis. To activate H-TaS$_2$ flakes for the HER, the morphology of H-TaS$_2$ films is texturized by a thermal treatment in a H$_2$-rich atmosphere. Our method is compared to the electrochemical treatment, namely, 1000 CV cycles, reported in the literature[40,41] and patent,[47] to design an efficient catalyst for the HER based on TMDs. Lastly, accordingly to ab initio molecular dynamic (AIMD) simulations and DFT calculations,[42] the H-TaS$_2$ flakes are hybridized with the H-TaSe$_2$ flakes (produced similarly to H-TaS$_2$ flakes) to tune the ΔG_H of the H-TaS$_2$ basal planes and edges in the resulting heterogeneous configurations toward the ideal close to zero value in acidic media. In agreement with the theoretical expectations, in acidic media (0.5 M H$_2$SO$_4$), the proposed heterogeneous catalysts, based only on group 5 TMDs, outperform their single counterparts. In addition, the heterogeneous catalysts exhibit a high mass activity of 314 A g^{-1} at an overpotential of 200 mV, which is promising for practical applications. For the first time, the HER activity of these materials is investigated in alkaline media (1 M KOH), showing a η_{10} of 230 mV and a mass activity of 220 A g^{-1} at an overpotential of 300 mV (for the heterogeneous catalysts). The HER activity of the heterogeneous electrodes is demonstrated over several hours (12 h) of continuous operation at fixed potential corresponding to a starting current density of −80 mA cm^{-2}, proving their durability. Additional characterization after electrochemical tests provides new understanding on chemical modifications during operation of these catalysts for the HER. Our results furnish a novel guidance to use the metallic group 5 TMDs as efficient HER catalysts by means of scalable material preparation and electrode processing.

2. EXPERIMENTAL SECTION

2.1. Materials. Tantalum (99.9%, <100 μm), sulfur (99.999%, <6 mm), and selenium (99.999%, 2−4 mm) were purchased from Strem, USA. Sulfuric acid (99.999%), KOH (reagent grade, 90%, flakes), Pt/C (20 wt % loading), and Nafion solution (5 wt %) were supplied by Sigma-Aldrich. The single-walled carbon nanotubes (SWCNTs) (>90% purity) were supplied by Cheap Tubes.

2.2. Synthesis and Exfoliation of the Crystals. The 2H-TaS$_2$ and the 2H-TaSe$_2$ crystals were produced by direct synthesis from their composing elements. A quantity of Ta (10 g) and chalcogen powders with a Ta:S or Ta:Se stoichiometry of 1:2 was placed in a quartz glass container (20 mm × 120 mm). After reaching high vacuum (1 × 10^{-3} Pa), the container was heated to 450 °C for 12 h and then to 600 °C for 48 h. Lastly, the Ta dichalcogenides were treated at 900 °C for 48 h and cooled down at room temperature over 24 h. The H-TaS$_2$ and the H-TaSe$_2$ flakes were obtained through LPE,[48,49] followed by sedimentation-based separation (SBS), in 2-propanol (IPA) of the as-synthesized crystals. More in detail, 50 mg of fragmentized crystals was inserted in 50 mL of anhydrous IPA. The so-obtained mixture was ultrasonicated in a sonicator (Branson 5800 cleaner, Branson Ultrasonics) for 6 h. Afterward, the dispersion was ultracentrifuged using a Beckman Coulter centrifuge (Optima XE-90 with a SW32Ti rotor) at 2700g for 20 min at 15 °C in order to separate the

exfoliated materials in the supernatant from the unexfoliated bulk crystals, which was found as sediment. Finally, the exfoliated materials were collected by pipetting 80% of the supernatant, thus getting the exfoliated Ta dichalcogenide dispersion. The concentration of H-TaS$_2$ and H-TaSe$_2$ flake dispersions were 0.35 and 0.3 g L^{-1}, respectively.

2.3. Preparation of the Dispersions of the Exfoliated Materials. The dispersions of H-TaS$_2$ and H-TaSe$_2$ flakes were used as produced. The hybrid dispersions of H-TaS$_2$ and H-TaSe$_2$ flakes were produced by mixing the H-TaS$_2$ flakes and H-TaSe$_2$ flakes dispersions (material weight ratio of 1:1). The dispersion of SWCNTs in *N*-methyl-2-pyrrolidone (NMP) was produced following the protocols based on ultrasonication-based debundling,[50,51] as previously reported in the literature.[24,36,37,42] To produce the dispersion of Pt/C, 5 mg of Pt/C was dissolved in 950 μL of ethanol and 50 μL Nafion solution. The Pt/C dispersion was ultrasonicated for 5 min before being used.

2.4. Characterization of the Materials. Scanning electron microscopy (SEM) analysis of the as-synthesized crystal and the exfoliated materials was performed using a Helios Nanolab 600 DualBeam microscope (FEI Company) and 10 kV and 0.2 nA as measurement conditions. The energy-dispersive X-ray spectroscopy (EDS) spectra were acquired with a microscope combined with an X-Max detector and INCA system (Oxford Instruments) operating at 15 kV and 0.8 nA. The samples were imaged without any metal coating or pretreatment. Transmission electron microscopy (TEM) images were acquired with a JEM 1011 (JEOL) TEM (thermionic W filament) operating at 100 kV. ImageJ software (NIH) and OriginPro 9.1 software (OriginLab) were used to perform the morphological and statistical analyses, respectively. The samples were produced by depositing the exfoliated material dispersions onto ultrathin C-on-holey C-coated Cu grids. The grids were then rinsed with deionized water and subsequently dried overnight under vacuum. Atomic force microscopy (AFM) measurements were carried out using Nanowizard III (JPK Instruments, Germany) mounted on an Axio Observer D1 (Carl Zeiss, Germany) inverted optical microscope. The measurements were carried out using PPP-NCHR cantilevers (Nanosensors, USA) having a tip with a nominal diameter of 10 nm. A drive frequency of ∼295 kHz was used for image acquisition. The images were collected in intermittent contact mode over an area of 2.5 × 2.5 μm^2 (512 × 512 data points) using a scan rate of 0.7 Hz. The working set point was set above 70% of the free oscillation amplitude. The height profile analysis was performed using the JPK Data Processing software (JPK Instruments, Germany). OriginPro 9.1 software was used to perform the statistical analysis of the thickness of the flakes, which were visualized on multiple AFM images acquired for each sample. The samples were produced by depositing the exfoliated material dispersions on mica substrates (G250-1, Agar Scientific Ltd.). Before the measurements the samples were dried under vacuum overnight. PANalytical Empyrean using Cu Kα radiation was used to perform X-ray diffraction (XRD) measurements. The samples were produced by depositing the exfoliated material dispersions onto substrates of Si/SiO$_2$. Before the measurements, the samples were dried under vacuum overnight. Renishaw microRaman Invia 1000, mounting a 50× objective and using an excitation wavelength of 532 nm and an incident power on the samples of 1 mW, was used to carry out the Raman spectroscopy measurements. The samples were prepared by

depositing the exfoliated material dispersions onto substrates of Si/SiO$_2$. Before the measurements the samples were dried under vacuum overnight.

2.5. Fabrication of the Electrodes. The electrodes were fabricated by sequentially depositing the SWCNTs and exfoliated catalytic material (H-TaS$_2$, H-TaSe$_2$, and H-TaS$_2$:H-TaSe$_2$) dispersions onto commercial Whatman membrane filters (nylon with a pore size of 0.2 μm) through the vacuum filtration method (electrode area = 3.8 cm^2). The material mass loadings were ∼1.31 and ∼0.20 mg cm^{-2} for the SWCNTs and the exfoliated catalytic materials, respectively. Before the electrochemical measurements, the electrodes were dried at room temperature overnight. The electrodes were thermally treated in a quartz tube (inner diameter = 25 mm, length = 120 cm) placed in a 3-zone split furnace (PSC 12/−/600H, Lenton, UK). While keeping a 100 sccm flow of Ar(90):H$_2$(10) gas mixture through the tube, the electrodes were heated at 600 °C with a ramp of 12 °C min^{-1} for 3 h. An array of mass flow controllers (1479A, mks, USA) was used to control upstream the flow of the gases. Lastly, the furnace was switched off, and the quartz tube was cooled down to room temperature. Electrodes made entirely of SWCNTs were also produced as reference. The electrodes of Pt/C were fabricated by drop casting the Pt/C dispersion onto cleaned glassy carbon (GC) sheets. The mass loading of Pt/C was 0.354 mg cm^{-2}.

2.6. Characterization of the Electrodes. The SEM imaging of the as-produced electrodes and the electrodes after CV cycling was performed using the microscope and the parameters reported for material characterization. The SEM-coupled EDS analysis of the electrodes was performed using a field-emission scanning electron microscope (JEOL JSM-6490LA SEM). The acceleration voltage was set to 25 kV. X-ray diffraction measurements were acquired with a PANalytical Empyrean using Cu Kα radiation. The electrochemical measurements of the electrodes were performed using a VMP3 multichannel potentiostat/galvanostat (Bio-Logic) controlled via Bio-Logic's own software. The measurements were carried out in a three-electrode configuration at room temperature and using a footed 250 mL quartz cell with dual flat windows (Pine Research) as the electrochemical cell. A KCl-saturated Ag/AgCl and a carbon rod and were used as the reference electrode and the counter electrode, respectively. The measurements were performed in acid (0.5 M H$_2$SO$_4$) or alkaline (1 M KOH) media (medium volume = 200 mL). Inductively coupled plasma optical emission spectroscopy (ICP-OES) measurements were carried out to evaluate the contamination in the KOH reagent. These measurements were carried out using an iCAP 6000 Duo (Thermo Fisher Scientific) on a sample prepared by digesting 25 mg of KOH in 2.5 mL of HCl:HNO$_3$ (3:1 vol/vol) overnight. Before starting the electrochemical measurements, N$_2$ gas was flowed throughout the liquid media using a porous frit in order to remove the dissolved O$_2$. The applied/measured potentials vs Ag/AgCl were converted to the reversible hydrogen electrode (RHE) scale according to the Nernst equation $E_{RHE} = E_{Ag/AgCl} + 0.059 \times pH + E^0_{Ag/AgCl}$ in which E_{RHE} is the potential vs the RHE, $E_{Ag/AgCl}$ is the potential vs the Ag/AgCl reference electrode, and $E^0_{Ag/AgCl}$ is the standard potential of the Ag/AgCl reference electrode at 25 °C (0.1976 V vs. RHE). The LSV curves were measured using a potential scan rate of 5 mV s^{-1}. The LSV data were *iR* corrected (100% *iR*-drop compensation) by considering *i* as the measured working electrode current and *R* as the series resistance of the resistance
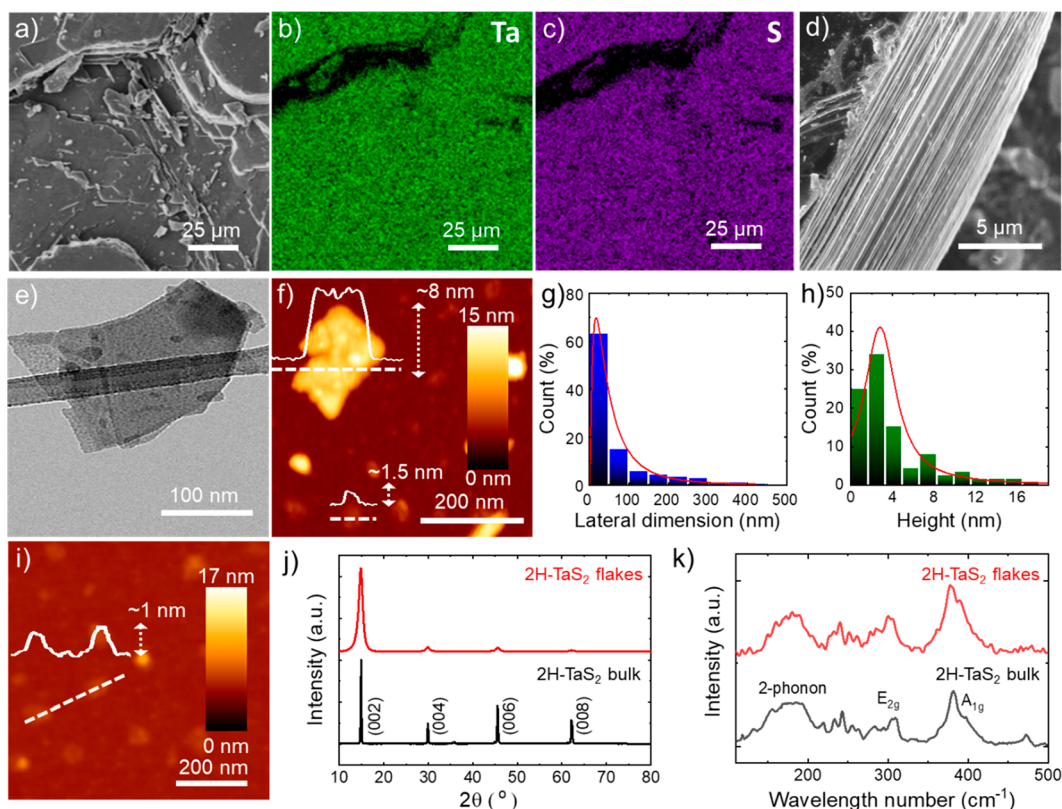
Figure 2. (a) SEM image of as-synthesized 2H-TaS$_2$ crystals with corresponding EDS maps for (b) Ta (Lα = 8.14 keV) and (c) S (Kα = 2.3 keV). (d) High-magnification SEM image of an edge of a representative 2H-TaS$_2$ crystal, evidencing its layered structure. (e) TEM image of representative H-TaS$_2$ flakes. (f) Representative AFM image of representative H-TaS$_2$ flakes. (g) Statistical analysis of the lateral dimension of H-TaS$_2$ flakes. (h) Statistical analysis of H-TaS$_2$ flakes. (i) AFM image of H-TaS$_2$ flakes, showing the presence of monolayer 1H-TaS$_2$ flakes. (j) XRD and (k) Raman spectra of the as-produced 2H-TaS$_2$ bulk crystals and H-TaS$_2$ flakes.

of the electrolyte and the resistance of the substrate of the working electrode. R was measured through electrochemical impedance spectroscopy (EIS) measurements at open-circuit potential and using a frequency of 10 kHz. The mass activity of the catalytic films was evaluated by the ratio between the current density measured at fixed potential and the catalyst mass loading. The mass loading of the catalysts was approximated to that of the electrode before any kind of treatments. Chronoamperometry measurements were carried to evaluate the stability of the electrodes. The overpotential was set to provide an initial cathodic current density of 80 mA cm^{-2}. An alkaline-resistant flat-bottom polytetrafluoroethylene (PTFE) (Pine Research) cell was used for the stability tests in alkaline media in order to exclude quartz dissolution effects on the electrode performance.

3. RESULTS AND DISCUSSION

3.1. Production and Characterization of H-TaS$_2$ Flakes.
The 2H-TaS$_2$ crystals were synthesized by the direct reaction from elements using Ta powder and S granules in a quartz glass ampule (see Experimental Section for the details). After reaction, the products were cooled down slowly in order to stabilize the 2H phase. Scanning electron microscopy-coupled EDS measurements of the as-synthesized 2H-TaS$_2$ crystals (Figure 2a−c) indicate a near-ideal stoichiometric phase of the 2H-TaS$_2$ crystals (S-to-Ta atomic % ratio = 1.9, see Supporting Information, Table S1), as expected from previous studies.[45,52] The high-magnification SEM image

(Figure 2d) of the edges of a crystal clearly evidence the layered structure expected for 2H-TaS$_2$.

The H-TaS$_2$ flakes were produced by LPE[48,49] of the synthesized crystals in IPA followed by SBS[53,54] to remove the unexfoliated material (see Experimental Section for additional details). Our approach aimed to provide a scalable method to produce nanostructured H-TaS$_2$ starting from cost-effective synthesized crystals and without resorting time-consuming bottom-up nanomaterial synthesis, such as CVD, or complex processing of materials.[55]

The morphology of H-TaS$_2$ flakes was characterized by TEM and AFM. Figure 2e reports the TEM image of representative H-TaS$_2$ flakes, which show irregularly shaped wrinkled structures. An AFM image of the H-TaS$_2$ flakes is shown in Figure 2f, together with the height profiles of two individual 2H-TaS$_2$ flakes with thicknesses of ∼1.5 and ∼8 nm, respectively. Statistical TEM analysis of the lateral dimension of the flakes (Figure 2g) shows values in the range of 10−450 nm, mainly distributed at values < 100 nm (log-normal distribution peaks at ∼30 nm). The statistical AFM analysis of the thickness of the flakes (Figure 2h) indicates that the sample is mainly made of few-layer 2H-TaS$_2$ flakes (AFM thickness of a TaS$_2$ monolayer is typically between 0.4 and 0.9 nm).[56−58] Their thickness follows a log-normal distribution peak at ∼2.8 nm. The 1H-TaS$_2$ monolayers have also been observed in the exfoliated sample, as reported in the AFM image shown in Figure 2i.

The metallic H phase of the TaS$_2$ flakes was confirmed by XRD measurements (Figure 2j) as indexed by ICSD-
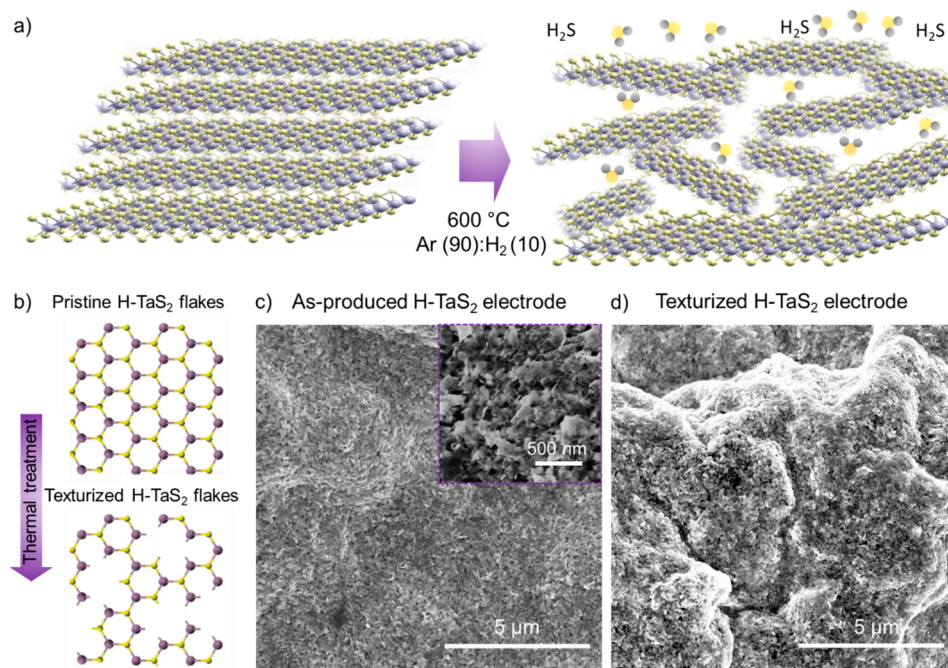
Figure 3. (a) Schematic illustration of the H_2S-aided texturization of the $H\text{-}TaS_2$ electrodes treated at 600 °C in H_2-rich environment (Ar(90):H_2(10) atmosphere). During this process, molecular H_2 reacts with t$H\text{-}TaS_2$ flakes and the S atoms are removed as H_2S (in form of gas). Evolved H_2S gas perforates and peels away the $H\text{-}TaS_2$ flakes, causing a laminar-to-porous conversion of the electrode structure. (b) Sketch of the texturization at "flake level" in which the evolution of H_2S gas enriches the number of highly HER active Ta edges. (c and d) Top-view SEM images of the $H\text{-}TaS_2$ electrode before and after the thermal treatment at 600 °C in Ar(90):H_2(10) atmosphere. (Inset to c) Enlargement of the surface of the as-produced $H\text{-}TaS_2$ electrodes, evidencing the flake-composed laminar structure.

651082.[52,59] For the $H\text{-}TaS_2$ flakes, the (002) peak is broader (full width half-maximum (fwhm) = 1.06°) than that of the synthesized 2$H\text{-}TaS_2$ crystal (fwhm = 0.18°). The broadening of the XRD peak could be related to the extent of the crystalline domain (the broader the peak, the smaller the crystalline domain). Therefore, it indicates the successful exfoliation of the sample. The other reflections are strongly reduced in intensity, although they retain their native position. This means that the $H\text{-}TaS_2$ flakes preserve their native crystal structure while orienting with their c axis perpendicular to the substrate.[34,60] Raman spectroscopy measurements (Figure 2k) further confirm the crystallinity retention of the exfoliated sample, which exhibits the same Raman modes of the native crystal (e.g., the out-of-plane vibration mode A_{1g} at ~380 cm^{-1}, the in-plane vibrational mode E^1_{2g} at ~300 cm^{-1}, and the broad second-order peak attributed to a two-phonon process at ~180 cm^{-1}).[61,62]

3.2. $H\text{-}TaS_2$ Electrode Fabrication and Characterization. To take advantage of the production of the $H\text{-}TaS_2$ flakes through LPE in dispersion form, the electrodes were obtained by sequential vacuum filtration of SWCNT and $H\text{-}TaS_2$ flake (material mass loading of ~1.31 and ~0.20 mg cm^{-2} for SWCNTs and $H\text{-}TaS_2$ flakes, respectively) through nylon filters (then used as electrode support). The production of the SWCNT dispersion and the protocol used to fabricate the electrodes are in agreement with our previous studies on TMDs-based catalysts (see Experimental Section for further description).[34−37,63] Noteworthy, our electrode manufacturing approach is particularly effective for one/two-dimensional materials since it does not lead to any material losses (different from the case of noble-metal nanoparticles typically used as catalysts).[36,37] Moreover, the choice of a SWCNT film (i.e., buckypaper) as the substrate relies on our previous findings

showing that the porosity of such substrate promotes the adhesion of a TMD flake film without the need of ion-conducting catalyst binders.[24,36,37,64]

In order to resemble the self-optimizing texturization of the $H\text{-}TaS_2$ films previously reported by electrochemical treatments (i.e., CV cycling),[40,41,44] where H_2 evolving from the TMD basal planes causes catalyst fracturing, our electrodes have been thermally treated in a H_2-rich environment at 600 °C (Figure 3a) (the resulting sample is herein named $H\text{-}TaS_2$-Ar/H_2@600°C). In fact, during this process, the molecular H_2 reacts with the $H\text{-}TaS_2$ flakes and S atoms are removed as H_2S (in the form of gas) (Figure 3b).[33] Beyond the formation of HER active Ta edges, the H_2S gas evolving from the basal planes perforates or peels away $H\text{-}TaS_2$ layers. Consequently, this effect increases the porosity and the electrochemically accessible surface area of the electrode films.[64,65] Double-layer capacitance (C_{dl}) measurements of the $H\text{-}TaS_2$ films (deposited on flat GC substrates in order to exclude the capacitive contribution of SWCTNs) before and after the thermal treatment were performed to confirm the effect attributed to the thermal treatments (Figure S1). These data show that the thermal treatments significantly increase (by +39%) the C_{dl} of the electrodes, which means that their electrochemically accessible surface area also increases. Moreover, EDS measurements of the $H\text{-}TaS_2$ electrodes show an ~14% reduction of the S content after the thermal treatment, corroborating the S removal from the $H\text{-}TaS_2$ flakes via the H_2S evolution process. The top-view SEM images of the electrode before and after the thermal treatment (Figure 3c and 3d) also confirm the above-discussed morphology evolution of the $H\text{-}TaS_2$ film. By doing so, the H_2S evolution-aided texturization partially resembles the H_2 evolution-aided one performed by the in-operando electro-

chemical approach.[40,41] However, our method does not require time-consuming electrochemical conditioning and simultaneously creates highly HER active metallic edges. In addition to the morphology changes, XRD measurements reveal the formation of oxides (i.e., Ta_2O_5) onto the surface of thermally treated H-TaS_2 films (Figure S2). In agreement with previous studies on other TMDs (namely, 2H-MoS_2),[65] the chalcogen loss can lead to the formation of elemental metal, which subsequently oxidizes when it is exposed to air. Moreover, surface-sensitive grazing angle XRD measurements have shown that this process mainly affects the surface of the material in contact with H_2-rich atmosphere, while the remaining material can preserve its chemical properties,[65] allowing the flakes to not drastically evolve from a two-dimensional morphology to cluster-like structures (caused by metal coalescence), in agreement with our SEM analysis (Figure 3).

The HER activity of the H-TaS_2 electrodes was investigated in either acidic (0.5 M H_2SO_4) or alkaline (1 M KOH) N_2-purged solutions at a temperature of 22 °C (room temperature). To the best of our knowledge, the HER activity of the Ta dichalcogenides in alkaline conditions was not studied neither theoretically nor experimentally. Figure 4a and 4b
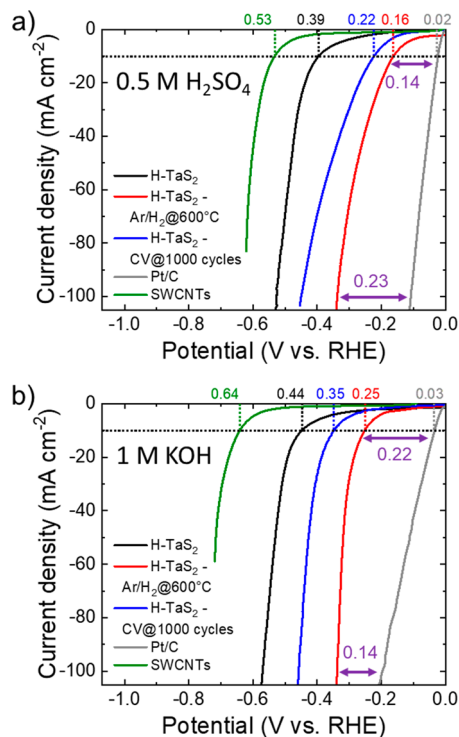

Figure 4. (a and b) *iR*-corrected LSV curves measured for H-TaS_2, H-TaS_2-Ar/H_2@600°C, and H-TaS_2-CV@1000 cycles in 0.5 M H_2SO_4 and 1 M KOH, respectively. LSV curves measured for the SWCNTs (catalyst support) and the Pt/C (benchmark) are also plotted for comparison. η_{10} values measured for the electrodes are indicated. For H-TaS_2-Ar/H_2@600°C, the HER overpotentials vs the overpotential of Pt/C at 10 and 100 mA cm² are also shown.

shows the *iR*-corrected linear sweep voltammetry (LSV) curves in 0.5 M H_2SO_4 and 1 M KOH, respectively, for the investigated electrodes before and after the thermal treatment (samples named H-TaS_2 and H-TaS_2-Ar/H_2@600°C, respectively). Moreover, the LSV curves measured for the electrochemically treated electrode (i.e., nonthermally treated electrode after 1000 CV cycles, sample named H-TaS_2-CV@

1000 cycles), the SWCNTs (catalyst support), and the Pt/C (benchmark) are also shown. In 0.5 M H_2SO_4, H-TaS_2-Ar/H_2@600°C exhibits a HER activity significantly higher than that of the as-produced electrodes (H-TaS_2). In particular, H-TaS_2-Ar/H_2@600°C shows a η_{10} of 160 mV, which is also inferior to that of the H-TaS_2-CV@1000 cycles (η_{10} = 220 mV). Similar results were measured in 1 M KOH, in which H-TaS_2-Ar/H_2@600°C shows a η_{10} of 250 mV, whereas the as-produced H-TaS_2 and H-TaS_2-CV@1000 cycles display a η_{10} of 440 and 350 mV, respectively. A thorough analysis of the HER kinetics, including the extrapolation of both the Tafel slope and the exchange current, was not carried out in this work because misleading interpretations can derive from the presence of the highly porous SWCNTs as the support of our catalytic films. In fact, SWCNTs have a high electrochemically accessible surface area that causes a significant capacitive current density (in the order of 1 or 10 mA cm⁻²) even at low potential scan rate (i.e., <10 mV s⁻¹).[36] Such capacitive contribution of the substrate is often the cause of mistakes, since it makes the correct evaluation of the kinetic parameters through standard protocols hard (see further details above in the text, section 3.4, which will specifically discuss the intrinsic catalytic properties of our electrodes).[66,67] Noteworthy, the differences between the HER overpotential of the Pt/C and the H-TaS_2-Ar/H_2@600°C electrode at a current density of 100 mA cm⁻² is as low as 230 and 0.140 mV in 0.5 MH_2SO_4 and 1 M KOH, respectively. In agreement with previous studies on group 5 TMDs,[68] these results indicate that our electrodes may optimally operate at high current densities, such as those required in real electrolyzers. Moreover, our results agree with the recent DFT simulations,[25,45] which show that the atomic H binding for both Ta and S edges (displaying ΔG_H < 0 eV at low atomic H coverage, i.e., ≤25%, see also Figure 1) weakens incrementally with increasing H coverage, leading to ideal-like ΔG_H close to 0 eV. Overall, our data suggests that H-TaS_2 flakes may be efficient and scalable HER catalysts.

3.3. H-TaS_2:H-$TaSe_2$ Heterogeneous Catalysts. To further utilize the potential of group 5 TMDs for the HER, H-TaS_2 flakes were hybridized with the $TaSe_2$ flakes to tune the ΔG_H of resulting heterogeneous configurations to optimal close to zero values for both the edges and the basal planes of the flakes. Although the theoretical HER activity of Se-based group 5 TMD has been shown to be lower than that of S-based counterparts,[40] recent DFT simulations and AIMD simulations[42] revealed that the heterogeneous stacking of Se- and S-based group 5-TMDs can increase the HER activity of S-based parts. Particularly for the case of Ta-based TMDs, the stacking promotes an electron transfer from H-$TaSe_2$ flakes to H-TaS_2 flakes (Figure 5a), decreasing the standard ΔG_H of the H-TaS_2 basal plane (>0.1 eV) toward 0 eV (Figure 5b).[42] Although the standard ΔG_H of the basal planes of stacked H-TaS_2 flakes might still be higher than 0 eV (and higher than the nearly zero standard ΔG_H of the edge sites), the abundance of the HER active sites associated with their basal planes could promote the HER activity at high H coverage conditions (i.e., high current density). This effect could make such heterogeneous catalysts competitive with metallic catalyst benchmarks, including Pt/C.[42] In addition, the hybridization approach can preserve the scalability of the catalysts preparation, since it does not require in any complex morphological/structural chemical modifications, such as the chemical doping of
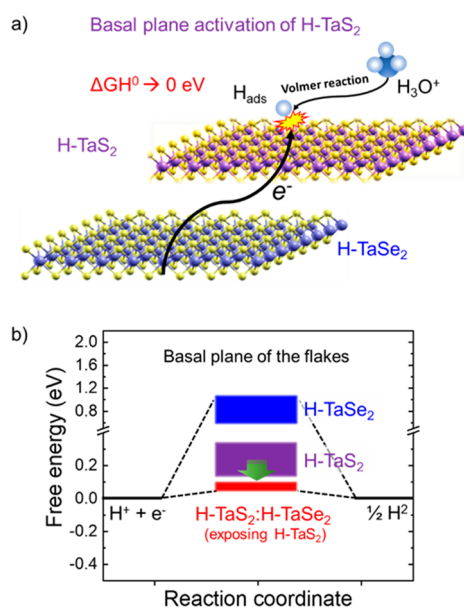
Figure 5. (a) Schematic illustration of the activation of the H-TaS$_2$ flakes for the HER in 0.5 M H$_2$SO$_4$ via the hybridization of H-TaS$_2$ and H-TaSe$_2$ flakes. Hybridization process fosters an electron transfer from H-TaSe$_2$ flakes toward H-TaSe$_2$ flakes, decreasing the standard ΔG_H value of the basal plane of H-TaS$_2$ flakes toward 0 eV. This effect promotes the first step of the HER (Volmer reaction, i.e., H$_3$O$^+$ + e$^-$ ⇄ H$_{ads}$ + H$_2$O). (b) Evolution of the standard ΔG_H for the basal planes of H-TaS$_2$, H-TaSe$_2$ flakes, and H-TaS$_2$:H-TaSe$_2$ heterogeneous catalysts. Rectangles are used to indicate data ranges that have been extrapolated from the literature for the standard ΔG_H (ref 42).

heteroatoms, the creation of artificial defects, or the strain impositions.[42]

The details regarding the synthesis of the 2H-TaSe$_2$ crystals are reported in the Experimental Section. Figure S3a−c shows the SEM-coupled EDS analysis of the as-synthesized 2H-TaSe$_2$ crystal, revealing a near-ideal stoichiometric phase (Se to Ta atomic % ratio = 2.2, see Table S2), which agrees with the previous literature.[45,52] The layered structure of the 2H-TaSe$_2$ crystals is evidenced on its edges, as proven by a representative high-magnification SEM image (Figure S2d). The H-TaSe$_2$ flakes were produced through LPE of fragmentized 2H-TaSe$_2$ crystals in IPA, following the same protocol used for the exfoliation of 2H-TaS$_2$ crystals. Transmission electron microscopy (Figure S4) and SEM-coupled EDS (Figure S5) analyses show that the exfoliated sample consists of H-TaSe$_2$ flakes and one-dimensional trigonal Se byproducts. The latter are formed by the dissolution−recrystallization mechanism involving polycrystalline Se,[69−71] whose excess has been also detected in the as-synthesized crystals (see Figure S3).

Following the protocols used for H-TaS$_2$ electrodes, H-TaSe$_2$ and heterogeneous H-TaSe$_2$:H-TaS$_2$ (material mass ratio of 1:1) electrodes (hereafter named H-TaSe$_2$ and H-TaSe$_2$:H-TaS$_2$) were fabricated through vacuum filtration of their dispersions onto SWCNTs. Figure S6 reports representative SEM images of the H-TaSe$_2$ and H-TaSe$_2$:H-TaS$_2$ electrodes. The as-produced electrodes display a wrinkled structure, which is different from the laminar one shown for the H-TaS$_2$ electrodes. In fact, the whiskers in the exfoliated H-TaSe$_2$ sample modify the arrangement of the flakes during their film deposition. Although it is realistic to suppose that the vacuum filtration deposition of a dispersion of a mixture of H-TaS$_2$ and H-TaSe$_2$ nanoflakes naturally leads to the formation

of some stacks between nanoflakes of different materials, SEM-coupled EDS measurements were performed to demonstrate the absence of single-material domains. Top-view and cross-sectional SEM-coupled EDS analyses of the heterogeneous films composed by H-TaS$_2$ and H-TaSe$_2$ flakes (Figure S7) show homogeneous distributions for both S and Se, which indicates an optimum material mixing. Although our approach cannot accurately control the formation of heterogeneous configurations alternating flakes of different materials, we point out that it is promptly scalable and time saving compared to highly controlled nanofabrication methods. Moreover, for practical mass loadings, such as those used for our electrodes (i.e., 0.2 mg cm^{-2}), a highly controlled stacking of flakes of different materials is problematic with any method. Therefore, our method is convenient to design an efficient TMD-based electrode with a high mass loading of the catalysts. A similar approach has been recently used to make heterogeneous stacking between H-NbS$_2$ and H-MoSe$_2$ flakes to design heterogeneous catalysts with HER performance superior to those of the single catalytic counterpart.[43]

The thermal treatment of H-TaSe$_2$-based electrodes in a H$_2$-rich environment at 600 °C causes the evolution of H$_2$Se (in form of gas), in agreement with previous studies on another Se-based TMD (i.e., H-MoSe$_2$).[64] Therefore, the effects of the thermal treatment on H-TaSe$_2$ electrodes resemble those occurring on H-TaS$_2$ electrodes (see Figure 3). Moreover, XRD measurements on H-TaSe$_2$ films reveal the presence of surface oxides after the thermal treatment (Figure S8), similarly to the case of H-TaS$_2$ or other TMDs (e.g., 2H-MoS$_2$).[65] Lastly, it is worth noticing that for H-TaSe$_2$ both Ta and Se edges have been theoretically predicted to be highly catalytic for the HER process, whereas the basal planes are deemed inactive (differently from the H-TaS$_2$).[20,38,39,64]

Figure 6a and 6b shows the LSV curves in 0.5 M H$_2$SO$_4$ and 1 M KOH, respectively, for the as-produced heterogeneous electrodes before and after the thermal treatment (samples named H-TaS$_2$: H-TaSe$_2$ and H-TaS$_2$:H-TaSe$_2$-Ar/H$_2$@ 600 °C). Furthermore, the LSV curves measured for the non-thermally treated electrode after 1000 CV cycles (sample named H-TaS$_2$:H-TaSe$_2$-CV@1000 cycles), the H-TaS$_2$ electrode (reference), and the Pt/C (benchmark) and are also plotted. Electrochemical characterization of the electrodes made of only H-TaSe$_2$ flakes before and after thermal or electrochemical treatments is reported in the Supporting Information (Figure S9). As predicted by theoretical DFT simulations (see Figure 1),[20,38,39] H-TaSe$_2$ electrodes exhibit relevant HER activities in both acidic and alkaline media. In particular, after thermal treatment, the electrodes show a η_{10} as low as 200 and 260 mV in 0.5 M H$_2$SO$_4$ and 1 M KOH, respectively. These HER activities can be attributed to the abundant Ta edges, as detected by the EDS analysis (Figure S5). The hybridization of H-TaS$_2$ and H-TaSe$_2$ flakes increases the HER activity of both H-TaS$_2$ and H-TaSe$_2$ electrodes. Similarly to the single counterparts, both thermal treatment and CV cycling enhance the HER activity of our heterogeneous electrodes. In acidic condition, H-TaS$_2$:H-TaSe$_2$-Ar/H$_2$@600°C exhibits a η_{10} of 120 mV, whereas the non-thermally treated heterogeneous electrode after 1000 CV cycles (i.e., H-TaS$_2$:H-TaSe$_2$-CV@1000 cycles) shows a slightly higher η_{10} (140 mV). In 1 M KOH, H-TaS$_2$:H-TaSe$_2$-Ar/H$_2$@600°C shows a η_{10} of 240 mV, which is similar to that of H-TaS$_2$:H-TaSe$_2$-CV@1000 cycles (230 mV). Interestingly, at the high current density of 100 mA cm^{-2},
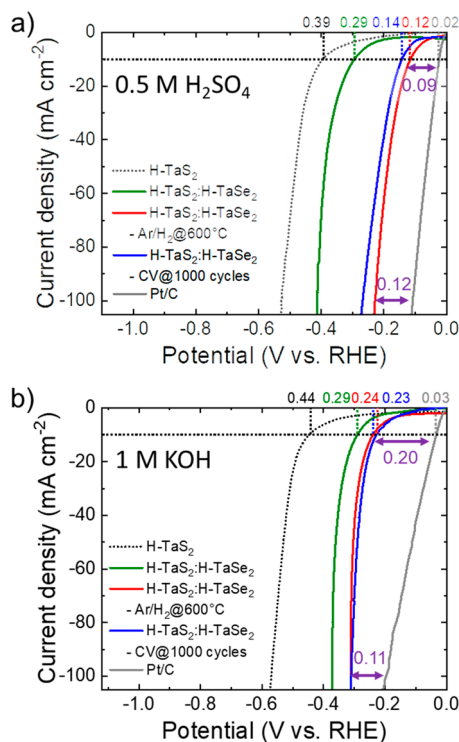
Figure 6. (a and b) *iR*-corrected LSV curves measured for H-TaS$_2$:H-TaSe$_2$, H-TaS$_2$:H-TaSe$_2$-Ar/H$_2$@600°C, and H-TaS$_2$:H-TaSe$_2$-CV@1000 cycles in 0.5 M H$_2$SO$_4$ and 1 M KOH solutions, respectively. LSV curves measured for Pt/C and H-TaS$_2$ (reference, dashed line) are also shown for comparison. η_{10} values measured for the electrodes are indicated. For H-TaS$_2$:H-TaSe$_2$-Ar/H$_2$@600°C, the HER overpotentials vs the overpotentials of Pt/C at 10 and 100 mA cm^{-2} are also shown.

the H-TaS$_2$:H-TaSe$_2$-Ar/H$_2$@600°C displays low HER overpotentials, only 120 and 110 mV higher than those of the Pt/C electrode in 0.5 M H$_2$SO$_4$ and 1 M KOH, respectively. Although the HER activity of our heterogeneous electrodes at low current density can still be mainly ascribed to the HER active edges of both H-TaS$_2$ and H-TaSe$_2$ flakes (in agreement with data shown in Figure 4 and Figure S9), the remarkable HER activity at high current density can be also associated with the hybridization-induced activation of the basal planes of H-TaS$_2$ flakes, as previously discussed in Figure 5.

Beyond the electrocatalytic activity, the durability of a catalyst is an essential requirement for its exploitation. Figure S10 reports the chronoamperometric measurements for our thermally treated electrodes (H-TaS$_2$:H-TaSe$_2$-Ar/H$_2$@600°C) at a potential corresponding to a starting current density of −80 mA cm^{-2} in both acidic and alkaline media. In 0.5 M H$_2$SO$_4$, H-TaS$_2$:H-TaSe$_2$-Ar/H$_2$@600°C maintained 97% of the starting current densities after 12 h, therefore proving an adequate HER activity durability. Interestingly, the durable HER activity of our electrodes has been reached without the use of any binder, such as Nafion, which could prospectively increase the mechanical strength of our electrodes as the HER proceeds. In fact, mechanical stress originated from H$_2$ bubbling has been shown to cause fragmentation of the group 5 TMDs.[40,41,47] As also shown in our experiments by treating electrodes with CV cycling, catalyst fragmentation initially improves the electrochemical performance of as-produced electrodes. However, they may also involve a significant loss of catalytic materials, which should be limited

for practical targets. Differently, our thermal treatment-aided texturization does not require any electrochemical conditioning of the electrodes, and the initial porosity of thermally treated electrodes could be advantageous to limit catalyst fragmentation effects while showing optimal HER activity from the beginning of operation. As shown by SEM analysis reported in Figure S11, H-TaS$_2$-Ar/H$_2$@600°C, in which the detection of thermo-induced texturization is easier than the one in heterogeneous electrodes, does not show any significant difference in the electrode morphology before and after CV cycling. On the contrary, the nonthermally treated electrode after 1000 CV cycles displays a fragmented surface, which is significantly different from the initial one. Noteworthy, SEM-coupled EDS analysis of our nonthermally treated heterogeneous electrodes also evidences morphology changes after CV cycling (Figure S12a). In addition, EDS mapping (Figure S12b−d) shows a slight redistribution of elements (especially for S), indicating the possibility of chemical changes at the electrode surface during HER. As shown in Figure S13, XRD measurements of H-TaS$_2$:H-TaSe$_2$-CV@1000 cycles further evidence chemical changes on its surface. In particular, the intensities of the Raman peaks attributed to oxides (i.e., Ta$_2$O$_5$) significantly increase compared to those observed in untreated samples (whose oxidation is marginal). At this stage, we cannot exclude the dissolution of the so-formed oxides in acidic media, as speculated in previous works.[41] The choice of proper electrochemical potential for carrying out HER could be considered to control both oxidation and dissolution effects, as shown in previous work on electrocatalysts.[72] Overall, we can state that our results partially contradict those previously reported for H-TaS$_2$ electrodes in the literature,[40,41] where it is claimed that H-TaS$_2$ preserves its chemical integrity. Therefore, additional specific studies on electrodes with catalyst mass loadings similar to those of our electrodes are still needed to definitively provide better understanding regarding possible chemical changes of this kind of catalyst in acidic media. In alkaline condition, the electrode degraded during the first 4 h; thereafter, the electrode's current density stabilized (current density equal to 81% of the initial one after 12 h) (see Figure S10). The stabilization of the current density suggests that an equilibrium between the catalytic properties and the electrochemical stability was also reached in alkaline condition. It is worth noticing that the dissolution of the quartz of the cell in alkaline media could alter the electrolyte composition, affecting the HER activity of the electrodes.[64,65] In order to exclude these effects, the stability tests were also carried out in a alkaline-resistant PTFE cell. As shown in Figure S14, these data confirm an initial degradation of the electrodes. Subsequently, the HER activity of the electrode progressively increases over time, suggesting an evolution toward an electrochemical equilibrium, which was also observed in the quartz cell. Elemental analysis of the KOH reagent used to prepare the 1 M KOH solution was also carried out through ICP-OES measurements to evaluate the presence of transition-metal and heavy-metal impurities, which could result in a misleading interpretation of the stability/durability of investigated electrodes.[73] Our data indicate that the content of metals (Fe, Co, Ni, Cu, Zn, Cd, Pb) is below the detection limit of the ICP equipment, agreeing with the product specification sheet provided by the material supplier (see Experimental Section for additional technical detail), i.e., Fe < 0.0005%, Zn ≤ 0.0005%, Co ≤ 0.0005%, Cu ≤ 0.0005%, and Pb ≤ 0.001%. These values suggest that the metallic impurities
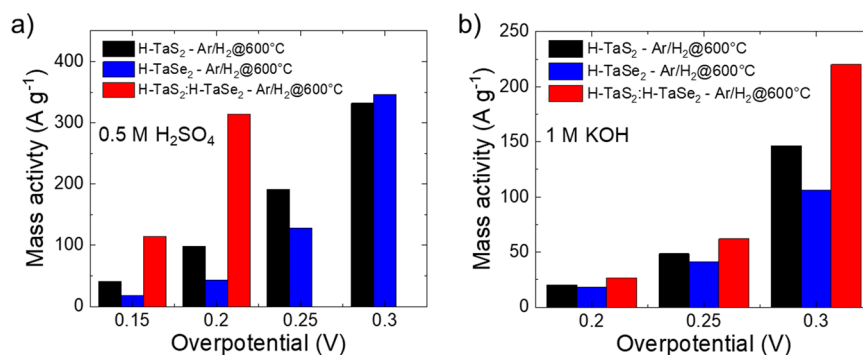
Figure 7. Mass activity of H-TaS$_2$-Ar/H$_2$@600°C, H-TaSe$_2$-Ar/H$_2$@600°C, and H-TaS$_2$:H-TaSe$_2$-Ar/H$_2$@600°C catalytic films at different overpotential (vs RHE) in (a) 0.5 M H$_2$SO$_4$ and (b) 1 M KOH.

are marginally affecting the HER activity of our electrodes, which are instead highly dependent by the electrode treatment proposed in this work. The chemical modification and/or dissolution of electrode materials could influence the HER activity durability of the investigated electrodes in alkaline media. Currently, we cannot rule out a possible oxidation of H-TaS$_2$ during HER operation in such conditions. Since the metallic Ta can oxidize in alkaline conditions,[66,67] oxidation processes could significantly impact the electrocatalyst metal edges, which are created during the thermal treatment of our electrodes (see Figure 3). Consequently, the initial degradation could be associated with these phenomena. Similar effects have been recently observed in other group 5 TMDs, i.e., H-NbS$_2$, in which a progressive oxidation of the surface of the flakes was also shown.[43] Moreover, it is worth pointing out that alkaline condition can promote the dissolution of oxidized Ta (e.g., Ta$_2$O$_5$), since it tends to form soluble oxotantalate (TaO)-(OH)$_x^{(3-x)+}$ and hydroxotantalate (TaO)(OH)$_x^{(5-x)+}$.[66,68] Consequently, a progressive reactivation of the electrode surface toward HER may explain the subsequent stabilization/increase of the HER activity of the electrodes, until the achievement of an electrochemical equilibrium. Lastly, hydr-(oxy)oxide species onto HER catalyst can also synergistically interact with the latter to modify the HER activity of the electrodes. In particular, it has been recently demonstrated that transition-metal oxides (or hydroxides) on a TMD surface can increase the HER activity of the pristine TMDs in alkaline media,[37,36,74,75] similarly to what is observed in noble metal-based electrocatalysts.[76–79] Therefore, the control of the oxidation effects, including those occurring during our thermal treatment (see Figurea S3 and S8), could be crucial for optimizing our current electrodes. Further measurements are still needed to unambiguously demonstrate the durability of Ta-based dichalcogenides in alkaline media. However, our preliminary results open the way toward the use of Ta-based dichalcogenides in electrolyte beyond the acidic ones, as recently reported for the most established HER active transition-metal dichalcogenides, including Mo-based ones.[24,36,37,74,80]

3.4. Evaluation of the Intrinsic Activity of the Catalysts.

In order to compare the catalytic performance of our electrocatalysts with those reported in the literature for similar materials, it is fundamental to evaluate the parameters that reflect the intrinsic electrocatalytic properties.[73,81,82] Since our catalytic films were deposited onto highly porous SWCNT films (i.e., buckypapers) as the substrates, the evaluation of the electrochemical surface area (hereafter denoted ECSA) of our

electrocatalysts through traditional methods used for TMD-based electrocatalysts (e.g., C_{dl} estimation through CV measurements at different scan rate in a nonfaradaic region)[83] can lead to overestimated values. Consequently, intrinsic catalytic performance normalized on ECSA would be seriously underestimated.[73,84] As shown in Figure S15, CV measurements evidence that the capacitance of SWCNTs obscures that of our catalytic films, thus impeding estimating the C_{dl} of our catalytic films. Although the C_{dl} of our catalytic films could be measured using flat substrates (as shown in Figure S1), the electrical contact between catalytic flakes and such substrates is not properly established, impeding a reliable quantitative ECSA analysis also in this case. Therefore, in agreement with literature recommendations,[82,84] we evaluate the intrinsic activity of our electrocatalysts by specifically focusing on the mass activity of our electrodes at various potentials. Figure 7a and 7b shows the mass activity of our thermally treated electrodes at various overpotentials ranging from 0.15 to 0.3 V in 0.5 M H$_2$SO$_4$ and from 0.2 to 0.3 in 1 M KOH (within these ranges, artifacts arising from the presence of capacitive contribution at low current densities are negligible). In 0.5 M H$_2$SO$_4$, H-TaS$_2$:H-TaSe$_2$-Ar/H$_2$@600°C displays a mass activity of the catalytic films of 114 and 314 A g^{-1} at overpotentials as low as 150 and 200 mV, respectively.

Table S3 reports a comparison between the geometric (η_{10}) and intrinsic performance (mass activity) of our heterogeneous electrodes with those previously reported in the literature with similar materials (for which the production method is also specified).[39–41,43,44,85–92] Our heterogeneous electrocatalysts reach performances significantly superior to MoS$_2$-based catalysts[29,93] and most of the group 5 TMDs reported in the literature, except for those produced by CVD methods and subsequently electrochemically treated with thousands of CV cycles[40] or doped with noble-metal atoms.[87,94] Therefore, our catalysts prove that it is possible to reach the performance predicted for group 5 TMDs with scalable and practical methods.

4. CONCLUSIONS

In summary, we produced single/few-layer flakes of H-TaS$_2$ and H-TaSe$_2$ through an eco-friendly liquid-phase exfoliation (LPE) of their crystals in 2-propanol. The as-produced flakes have been used in the form of films to catalyze the hydrogen evolution reaction (HER) in both acidic and alkaline media. More in detail, thermal treatment in a H$_2$-rich atmosphere has been used to texturize the morphology of the catalytic films, increasing their porosity and the number of the HER active

edges of the flakes. Our method has been compared to the prototypical electrochemical CV cycling process, as previously reported in the literature[40,41] and licensed documents.[47] As supported by ab initio molecular dynamic simulations and density functional theory calculations,[42] the H-TaS$_2$ flakes have been hybridized with the H-TaSe$_2$ flakes to tune the ΔG_H of the H-TaS$_2$ basal planes to the optimal thermo-neutral value in the resulting heterogeneous configurations. In 0.5 M H$_2$SO$_4$, the designed heterogeneous catalysts based on Ta dichalcogenides outperform their single counterparts, showing an overpotential at the cathodic current density of 10 mA cm^{-2} (η_{10}) of 120 mV and high mass activity of 314 A g^{-1} at an overpotential of 200 mV. In 1 M KOH, they show a η_{10} of 230 mV and a mass activity of 220 A g^{-1} at an overpotential of 300 mV. Our heterogeneous electrodes show a durable HER activity over 12 h of nonstop operation at a fixed potential corresponding to a starting current density of −80 mA cm^{-2}. Our results furnish new guidelines for the use of the metallic group 5 TMDs for the HER by means of scalable material preparation and electrode processing.

■ ASSOCIATED CONTENT

ⓢ Supporting Information

This material is available free of charge on the ACS Publication Web sites. The Supporting Information is available free of charge at https://pubs.acs.org/doi/10.1021/acscatal.9b03184.

> Supplementary SEM-coupled EDS analysis of the 2H-TaS$_2$ and 2H-TaSe$_2$ crystals; double-layer capacitance measurements of the H-TaS$_2$ films; TEM and SEM-coupled EDS analysis of the exfoliated H-TaSe$_2$ sample; SEM analysis of the H-TaSe$_2$ and H-TaS$_2$:H-TaSe$_2$ electrodes; electrochemical characterization of the H-TaSe$_2$ electrodes; electrochemical stability of the heterogeneous H-TaS$_2$:H-TaSe$_2$ electrodes (PDF)

■ AUTHOR INFORMATION

Corresponding Author

Francesco Bonaccorso − *Graphene Labs, Istituto Italiano di Tecnologia, 16163 Genova, Italy; BeDimensional Spa, 16163 Genova, Italy;* ⓞ orcid.org/0000-0001-7238-9420; Phone: +39 01071781795; Email: francesco.bonaccorso@iit.it

Authors

Leyla Najafi − *Graphene Labs, Istituto Italiano di Tecnologia, 16163 Genova, Italy*

Sebastiano Bellani − *Graphene Labs, Istituto Italiano di Tecnologia, 16163 Genova, Italy*

Reinier Oropesa-Nuñez − *BeDimensional Spa, 16163 Genova, Italy;* ⓞ orcid.org/0000-0002-9551-6565

Beatriz Martín-García − *Graphene Labs, Istituto Italiano di Tecnologia, 16163 Genova, Italy;* ⓞ orcid.org/0000-0001-7065-856X

Mirko Prato − *Materials Characterization Facility, Istituto Italiano di Tecnologia, 16163 Genova, Italy;* ⓞ orcid.org/0000-0002-2188-8059

Lea Pasquale − *Materials Characterization Facility, Istituto Italiano di Tecnologia, 16163 Genova, Italy*

Jaya-Kumar Panda − *Graphene Labs, Istituto Italiano di Tecnologia, 16163 Genova, Italy*

Petr Marvan − *Department of Inorganic Chemistry, University of Chemistry and Technology Prague, 166 28 Prague 6, Czech Republic*

Zdeněk Sofer − *Department of Inorganic Chemistry, University of Chemistry and Technology Prague, 166 28 Prague 6, Czech Republic;* ⓞ orcid.org/0000-0002-1391-4448

Complete contact information is available at:
https://pubs.acs.org/10.1021/acscatal.9b03184

Author Contributions

‡L.N. and S.B.: These authors contributed equally.

Author Contributions

The manuscript was written through contributions of all authors. All authors have given approval to the final version of the manuscript.

Notes

The authors declare no competing financial interest.

■ ACKNOWLEDGMENTS

■ REFERENCES

(1) Momirlan, M.; Veziroglu, T. N. The Properties of Hydrogen as Fuel Tomorrow in Sustainable Energy System for a Cleaner Planet. *Int. J. Hydrogen Energy* **2005**, *30*, 795−802.

(2) Lewis, N. S.; Nocera, D. G. Powering the Planet: Chemical Challenges in Solar Energy Utilization. *Proc. Natl. Acad. Sci. U. S. A.* **2006**, *103* (43), 15729−15735.

(3) Edwards, P. P.; Kuznetsov, V. L.; David, W. I. F.; Brandon, N. P. Hydrogen and Fuel Cells: Towards a Sustainable Energy Future. *Energy Policy* **2008**, *36*, 4356−4362.

(4) Ball, M.; Weeda, M. The Hydrogen Economy - Vision or Reality? *Int. J. Hydrogen Energy* **2015**, *40*, 7903.

(5) Moliner, R.; Lázaro, M. J.; Suelves, I. Analysis of the Strategies for Bridging the Gap towards the Hydrogen Economy. *Int. J. Hydrogen Energy* **2016**, *41*, 19500−19508.

(6) Cherevko, S.; Geiger, S.; Kasian, O.; Kulyk, N.; Grote, J.-P.; Savan, A.; Shrestha, B. R.; Merzlikin, S.; Breitbach, B.; Ludwig, A.; MayrhoferK, J. J. Oxygen and Hydrogen Evolution Reactions on Ru, RuO2, Ir, and IrO2 Thin Film Electrodes in Acidic and Alkaline Electrolytes: A Comparative Study on Activity and Stability. *Catal. Today* **2016**, *262*, 170−180.

(7) You, B.; Sun, Y. Innovative Strategies for Electrocatalytic Water Splitting. *Acc. Chem. Res.* **2018**, *51*, 1571−1580.

(8) Sheng, W.; Zhuang, Z.; Gao, M.; Zheng, J.; Chen, J. G.; Yan, Y. Correlating Hydrogen Oxidation and Evolution Activity on Platinum at Different PH with Measured Hydrogen Binding Energy. *Nat. Commun.* **2015**, *6*, 5848.

(9) Durst, J.; Simon, C.; Hasche, F.; Gasteiger, H. A. Hydrogen Oxidation and Evolution Reaction Kinetics on Carbon Supported Pt, Ir, Rh, and Pd Electrocatalysts in Acidic Media. *J. Electrochem. Soc.* **2015**, *162*, F190−F203.

(10) Dubouis, N.; Grimaud, A. The Hydrogen Evolution Reaction: From Material to Interfacial Descriptors. *Chem. Sci.* **2019**, *10*, 9165−9181.

(11) Morales-Guio, C. G.; Stern, L.-A.; Hu, X. Nanostructured Hydrotreating Catalysts for Electrochemical Hydrogen Evolution. *Chem. Soc. Rev.* **2014**, *43*, 6555−6569.

(12) Zeng, M.; Li, Y. Recent Advances in Heterogeneous Electrocatalysts for the Hydrogen Evolution Reaction. *J. Mater. Chem. A* **2015**, *3*, 14942−14962.

(13) Zou, X.; Zhang, Y. Noble Metal-Free Hydrogen Evolution Catalysts for Water Splitting. *Chem. Soc. Rev.* **2015**, *44*, 5148−5180.

(14) Najafi, L.; Bellani, S.; Oropesa-Nuñez, R.; Martín-García, B.; Prato, M.; Bonaccorso, F. Single-/Few-Layer Graphene as Long-Lasting Electrocatalyst for Hydrogen Evolution Reaction. *ACS Appl. Energy Mater.* **2019**, *2*, 5373−5379.

(15) Cao, Z.; Chen, Q.; Zhang, J.; Li, H.; Jiang, Y.; Shen, S.; Fu, G.; Lu, B.; Xie, Z.; Zheng, L. Platinum-Nickel Alloy Excavated Nano-Multipods with Hexagonal Close-Packed Structure and Superior Activity towards Hydrogen Evolution Reaction. *Nat. Commun.* **2017**, *8*, 15131.

(16) Liu, Z.; Qi, J.; Liu, M.; Zhang, S.; Fan, Q.; Liu, H.; Liu, K.; Zheng, H.; Yin, Y.; Gao, C. Aqueous Synthesis of Ultrathin Platinum/Non-Noble Metal Alloy Nanowires for Enhanced Hydrogen Evolution Activity. *Angew. Chem., Int. Ed.* **2018**, *57*, 11678−11682.

(17) Greeley, J.; Jaramillo, T. F.; Bonde, J.; Chorkendorff, I. B.; Nørskov, J. K. Computational High-Throughput Screening of Electrocatalytic Materials for Hydrogen Evolution. *Nat. Mater.* **2006**, *5*, 909−913.

(18) Xu, H.; Wei, J.; Zhang, K.; Shiraishi, Y.; Du, Y. Hierarchical NiMo Phosphide Nanosheets Strongly Anchored on Carbon Nanotubes as Robust Electrocatalysts for Overall Water Splitting. *ACS Appl. Mater. Interfaces* **2018**, *10*, 29647−29655.

(19) Chhowalla, M.; Liu, Z.; Zhang, H. Two-Dimensional Transition Metal Dichalcogenide (TMD) Nanosheets. *Chem. Soc. Rev.* **2015**, *44*, 2584−2586.

(20) Chhowalla, M.; Shin, H. S.; Eda, G.; Li, L.-J.; Loh, K. P.; Zhang, H. The Chemistry of Two-Dimensional Layered Transition Metal Dichalcogenide Nanosheets. *Nat. Chem.* **2013**, *5*, 263.

(21) Merki, D.; Hu, X. Recent Developments of Molybdenum and Tungsten Sulfides as Hydrogen Evolution Catalysts. *Energy Environ. Sci.* **2011**, *4*, 3878−3888.

(22) Pumera, M.; Sofer, Z.; Ambrosi, A. Layered Transition Metal Dichalcogenides for Electrochemical Energy Generation and Storage. *J. Mater. Chem. A* **2014**, *2*, 8981−8987.

(23) Shi, X.; Fields, M.; Park, J.; McEnaney, J. M.; Yan, H.; Zhang, Y.; Tsai, C.; Jaramillo, T. F.; Sinclair, R.; Nørskov, J. K.; et al. Rapid Flame Doping of Co to WS2 for Efficient Hydrogen Evolution. *Energy Environ. Sci.* **2018**, *11*, 2270−2277.

(24) Martín-García, B.; Spirito, D.; Bellani, S.; Prato, M.; Romano, V.; Polovitsyn, A.; Brescia, R.; Oropesa-Nuñez, R.; Najafi, L.; Ansaldo, A.; D'Angelo, G.; Pellegrini, V.; Krahne, R.; Moreels, I.; Bonaccorso, F. Extending the Colloidal Transition Metal Dichalcogenide Library to ReS2 Nanosheets for Application in Gas Sensing and Electrocatalysis. *Small* **2019**, *15*, 1904670.

(25) Tsai, C.; Chan, K.; Nørskov, J. K.; Abild-Pedersen, F. Theoretical Insights into the Hydrogen Evolution Activity of Layered Transition Metal Dichalcogenides. *Surf. Sci.* **2015**, *640*, 133−140.

(26) Hinnemann, B.; Moses, P. G.; Bonde, J.; Jørgensen, K. P.; Nielsen, J. H.; Horch, S.; Chorkendorff, I.; Nørskov, J. K. Biomimetic Hydrogen Evolution: MoS2 Nanoparticles as Catalyst for Hydrogen Evolution. *J. Am. Chem. Soc.* **2005**, *127*, 5308−5309.

(27) Jaramillo, T. F.; Jørgensen, K. P.; Bonde, J.; Nielsen, J. H.; Horch, S.; Chorkendorff, I. Identification of Active Edge Sites for Electrochemical H2 Evolution from MoS2 Nanocatalysts. *Science* **2007**, *317*, 100−102.

(28) Xie, J.; Zhang, H.; Li, S.; Wang, R.; Sun, X.; Zhou, M.; Zhou, J.; Lou, X. W. D.; Xie, Y. Defect-Rich MoS2 Ultrathin Nanosheets with Additional Active Edge Sites for Enhanced Electrocatalytic Hydrogen Evolution. *Adv. Mater.* **2013**, *25*, 5807−5813.

(29) Kibsgaard, J.; Chen, Z.; Reinecke, B. N.; Jaramillo, T. F. Engineering the Surface Structure of MoS2 to Preferentially Expose Active Edge Sites for Electrocatalysis. *Nat. Mater.* **2012**, *11*, 963.

(30) Miao, M.; Pan, J.; He, T.; Yan, Y.; Xia, B. Y.; Wang, X. Molybdenum Carbide-Based Electrocatalysts for Hydrogen Evolution Reaction. *Chem. - Eur. J.* **2017**, *23*, 10947−10961.

(31) Seh, Z. W.; Fredrickson, K. D.; Anasori, B.; Kibsgaard, J.; Strickler, A. L.; Lukatskaya, M. R.; Gogotsi, Y.; Jaramillo, T. F.; Vojvodic, A. Two-Dimensional Molybdenum Carbide (MXene) as an Efficient Electrocatalyst for Hydrogen Evolution. *ACS Energy Lett.* **2016**, *1*, 589−594.

(32) Huang, Y.; Miao, Y.-E.; Fu, J.; Mo, S.; Wei, C.; Liu, T. Perpendicularly Oriented Few-Layer MoSe2 on SnO2 Nanotubes for Efficient Hydrogen Evolution Reaction. *J. Mater. Chem. A* **2015**, *3*, 16263−16271.

(33) Ye, G.; Gong, Y.; Lin, J.; Li, B.; He, Y.; Pantelides, S. T.; Zhou, W.; Vajtai, R.; Ajayan, P. M. Defects Engineered Monolayer MoS2 for Improved Hydrogen Evolution Reaction. *Nano Lett.* **2016**, *16*, 1097−1103.

(34) Najafi, L.; Bellani, S.; Martín-García, B.; Oropesa-Nuñez, R.; Del Rio Castillo, A. E.; Prato, M.; Moreels, I.; Bonaccorso, F. Solution-Processed Hybrid Graphene Flake/2H-MoS2 Quantum Dot Heterostructures for Efficient Electrocatalytic Hydrogen Evolution. *Chem. Mater.* **2017**, *29*, 5782−5786.

(35) Li, L.; Qin, Z.; Ries, L.; Hong, S.; Michel, T.; Yang, J.; Salameh, C.; Bechelany, M.; Miele, P.; Kaplan, D.; Chhowalla, M. Role of Sulfur Vacancies and Undercoordinated Mo Regions in MoS2 Nanosheets Towards the Evolution of Hydrogen. *ACS Nano* **2019**, *13*, 6824−6834.

(36) Najafi, L.; Bellani, S.; Oropesa-Nuñez, R.; Ansaldo, A.; Prato, M.; Del Rio Castillo, A. E.; Bonaccorso, F. Doped-MoSe2 Nanoflakes/3d Metal Oxide−Hydr(Oxy)Oxides Hybrid Catalysts for PH-Universal Electrochemical Hydrogen Evolution Reaction. *Adv. Energy Mater.* **2018**, *8*, 1801764.

(37) Najafi, L.; Bellani, S.; Oropesa-Nuñez, R.; Prato, M.; Martín-García, B.; Brescia, R.; Bonaccorso, F. Carbon Nanotube-Supported MoSe2 Holey Flake:Mo2C Ball Hybrids for Bifunctional PH-Universal Water Splitting. *ACS Nano* **2019**, *13*, 3162−3176.

(38) Zhu, C.; Gao, D.; Ding, J.; Chao, D.; Wang, J. TMD-Based Highly Efficient Electrocatalysts Developed by Combined Computational and Experimental Approaches. *Chem. Soc. Rev.* **2018**, *47*, 4332−4356.

(39) Huan, Y.; Shi, J.; Zou, X.; Gong, Y.; Zhang, Z.; Li, M.; Zhao, L.; Xu, R.; Jiang, S.; Zhou, X.; Hong, M.; Xie, C.; Li, H.; Lang, X.; Zhang, Q.; Gu, L.; Yan, X.; Zhang, Y. Vertical 1T-TaS2 Synthesis on Nanoporous Gold for High-Performance Electrocatalytic Applications. *Adv. Mater.* **2018**, *30*, 1705916.

(40) Liu, Y.; Wu, J.; Hackenberg, K. P.; Zhang, J.; Wang, Y. M.; Yang, Y.; Keyshar, K.; Gu, J.; Ogitsu, T.; Vajtai, R.; Lou, J.; Ajayan, P. M.; Wood, B. C.; Yakobson, B. I. Self-Optimizing, Highly Surface-Active Layered Metal Dichalcogenide Catalysts for Hydrogen Evolution. *Nat. Energy* **2017**, *2*, 17127.

(41) Shi, J.; Wang, X.; Zhang, S.; Xiao, L.; Huan, Y.; Gong, Y.; Zhang, Z.; Li, Y.; Zhou, X.; Hong, M.; Fang, Q.; Zhang, Q.; Liu, X.; Gu, L.; Liu, Z.; Zhang, Y. Two-Dimensional Metallic Tantalum Disulfide as a Hydrogen Evolution Catalyst. *Nat. Commun.* **2017**, *8*, 958.

(42) Han, B.; Noh, S. H.; Choi, D.; Seo, M. H.; Kang, J.; Hwang, J. Tuning the Catalytic Activity of Heterogeneous Two-Dimensional Transition Metal Dichalcogenides for Hydrogen Evolution. *J. Mater. Chem. A* **2018**, *6*, 20005−20014.

(43) Najafi, L.; Bellani, S.; Oropesa-Nuñez, R.; Martín-García, B.; Prato, M.; Mazánek, V.; Debellis, D.; Lauciello, S.; Brescia, R.; Sofer, Z.; Bonaccorso, F. Niobium Disulphide (NbS2)-Based (Heteroge-

neous) Electrocatalysts for an Efficient Hydrogen Evolution Reaction. *J. Mater. Chem. A* **2019**, *7*, 25593−25608.

(44) Zhang, J.; Wu, J.; Zou, X.; Hackenberg, K.; Zhou, W.; Chen, W.; Yuan, J.; Keyshar, K.; Gupta, G.; Mohite, A.; Ajayan, P. M.; Lou, J. Discovering Superior Basal Plane Active Two-Dimensional Catalysts for Hydrogen Evolution. *Mater. Today* **2019**, *25*, 28−34.

(45) Chia, X.; Ambrosi, A.; Lazar, P.; Sofer, Z.; Pumera, M. Electrocatalysis of Layered Group 5 Metallic Transition Metal Dichalcogenides (MX2, M = V, Nb, and Ta; X = S, Se, and Te). *J. Mater. Chem. A* **2016**, *4*, 14241−14253.

(46) Chirdon, D. N.; Wu, Y. Hydrogen Evolution: Not Living on the Edge. *Nat. Energy* **2017**, *2*, 17132.

(47) Hackenberg, K.; Keyshar, K.; Wu, J.; Liu, Y.; Ajayan, P.; Wood, B.; Yakobson, B. Self-Improving Electrocatalysists for Gas Evolution Reactions. US 2016/0153098 A1, 2016.

(48) Bonaccorso, F.; Bartolotta, A.; Coleman, J. N.; Backes, C. 2D-Crystal-Based Functional Inks. *Adv. Mater.* **2016**, *28*, 6136−6166.

(49) Nicolosi, V.; Chhowalla, M.; Kanatzidis, M. G.; Strano, M. S.; Coleman, J. N. Liquid Exfoliation of Layered Materials. *Science* **2013**, *340*, 1226419.

(50) Bonaccorso, F.; Hasan, T.; Tan, P. H.; Sciascia, C.; Privitera, G.; Di Marco, G.; Gucciardi, P. G.; Ferrari, A. C. Density Gradient Ultracentrifugation of Nanotubes: Interplay of Bundling and Surfactants Encapsulation. *J. Phys. Chem. C* **2010**, *114*, 17267−17285.

(51) Hasan, T.; Tan, P. H.; Bonaccorso, F.; Rozhin, A. G.; Scardaci, V.; Milne, W. I.; Ferrari, A. C. Polymer-Assisted Isolation of Single Wall Carbon Nanotubes in Organic Solvents for Optical-Quality Nanotube-Polymer Composites. *J. Phys. Chem. C* **2008**, *112*, 20227−20232.

(52) Luxa, J.; Mazánek, V.; Pumera, M.; Lazar, P.; Sedmidubský, D.; Callisti, M.; Polcar, T.; Sofer, Z. 2H→1T Phase Engineering of Layered Tantalum Disulfides in Electrocatalysis: Oxygen Reduction Reaction. *Chem. - Eur. J.* **2017**, *23*, 8082−8091.

(53) Capasso, A.; Del Rio Castillo, A. E.; Sun, H.; Ansaldo, A.; Pellegrini, V.; Bonaccorso, F. Ink-Jet Printing of Graphene for Flexible Electronics: An Environmentally-Friendly Approach. *Solid State Commun.* **2015**, *224*, 53−63.

(54) Maragó, O. M.; Bonaccorso, F.; Saija, R.; Privitera, G.; Gucciardi, P. G.; Iatì, M. A.; Calogero, G.; Jones, P. H.; Borghese, F.; Denti, P.; Nicolosi, V.; Ferrari, A. C. Brownian Motion of Graphene. *ACS Nano* **2010**, *4*, 7515−7523.

(55) Bonaccorso, F.; Lombardo, A.; Hasan, T.; Sun, Z.; Colombo, L.; Ferrari, A. C. Production and Processing of Graphene and 2d Crystals. *Mater. Today* **2012**, *15*, 564−589.

(56) Hu, Y.; Hao, Q.; Zhu, B.; Li, B.; Gao, Z.; Wang, Y.; Tang, K. Toward Exploring the Structure of Monolayer to Few-Layer TaS2 by Efficient Ultrasound-Free Exfoliation. *Nanoscale Res. Lett.* **2018**, *13*, 20.

(57) Navarro-Moratalla, E.; Island, J. O.; Mañas-Valero, S.; Pinilla-Cienfuegos, E.; Castellanos-Gomez, A.; Quereda, J.; Rubio-Bollinger, G.; Chirolli, L.; Silva-Guillén, J. A.; Agraït, N.; Steele, G. A.; Guinea, F.; van der Zant, H. S. J.; Coronado, E. Enhanced Superconductivity in Atomically Thin TaS2. *Nat. Commun.* **2016**, *7*, 11043.

(58) Zeng, Z.; Tan, C.; Huang, X.; Bao, S.; Zhang, H. Growth of Noble Metal Nanoparticles on Single-Layer TiS2 and TaS2 Nanosheets for Hydrogen Evolution Reaction. *Energy Environ. Sci.* **2014**, *7*, 797−803.

(59) Patterson, A. L. The Scherrer Formula for X-Ray Particle Size Determination. *Phys. Rev.* **1939**, *56*, 978−982.

(60) Yue, N.; Weicheng, J.; Rongguo, W.; Guomin, D.; Yifan, H. Hybrid Nanostructures Combining Graphene−MoS2 Quantum Dots for Gas Sensing. *J. Mater. Chem. A* **2016**, *4*, 8198−8203.

(61) Sugai, S.; Murase, K.; Uchida, S.; Tanaka, S. Studies of Lattice Dynamics in 2H-TaS2 by Raman Scattering. *Solid State Commun.* **1981**, *40*, 399−401.

(62) Hangyo, M.; Nakashima, S.-I.; Mitsuishi, A. Raman Spectroscopic Studies of MX2-Type Layered Compounds. *Ferroelectrics* **1983**, *52*, 151−159.

(63) Petroni, E.; Lago, E.; Bellani, S.; Boukhvalov, D. W.; Politano, A.; Gürbulak, B.; Duman, S.; Prato, M.; Gentiluomo, S.; Oropesa-Nuñez, R.; Panda, J. K.; Toth, P. S.; Del Rio Castillo, A. E.; Pellegrini, V.; Bonaccorso, F. Liquid-Phase Exfoliated Indium−Selenide Flakes and Their Application in Hydrogen Evolution Reaction. *Small* **2018**, *14*, 1800749.

(64) Najafi, L.; Bellani, S.; Oropesa-Nuñez, R.; Ansaldo, A.; Prato, M.; Del Rio Castillo, A. E.; Bonaccorso, F. Engineered MoSe2-Based Heterostructures for Efficient Electrochemical Hydrogen Evolution Reaction. *Adv. Energy Mater.* **2018**, *8*, 1703212.

(65) Kiriya, D.; Lobaccaro, P.; Nyein, H. Y. Y.; Taheri, P.; Hettick, M.; Shiraki, H.; Sutter-Fella, C. M.; Zhao, P.; Gao, W.; Maboudian, R.; Ager, J. W. General Thermal Texturization Process of MoS2 for Efficient Electrocatalytic Hydrogen Evolution Reaction. *Nano Lett.* **2016**, *16*, 4047−4053.

(66) Staszak-Jirkovský, J.; Malliakas, C. D.; Lopes, P. P.; Danilovic, N.; Kota, S. S.; Chang, K.-C.; Genorio, B.; Strmcnik, D.; Stamenkovic, V. R.; Kanatzidis, M. G.; Markovic, N. M. Design of Active and Stable Co−Mo−Sx Chalcogels as PH-Universal Catalysts for the Hydrogen Evolution Reaction. *Nat. Mater.* **2016**, *15*, 197.

(67) Shinagawa, T.; Garcia-Esparza, A. T.; Takanabe, K. Insight on Tafel Slopes from a Microkinetic Analysis of Aqueous Electrocatalysis for Energy Conversion. *Sci. Rep.* **2015**, *5*, 13801.

(68) Yang, J.; Mohmad, A. R.; Wang, Y.; Fullon, R.; Song, X.; Zhao, F.; Bozkurt, I.; Augustin, M.; Santos, E. J. G.; Shin, H. S.; Zhang, W.; Voiry, D.; Jeong, H. Y.; Chhowalla, M. Ultrahigh-Current-Density Niobium Disulfide Catalysts for Hydrogen Evolution. *Nat. Mater.* **2019**, *18*, 1309−1314.

(69) Murphy, K. E.; Altman, M. B.; Wunderlich, B. The Monoclinic◻to◻trigonal Transformation in Selenium. *J. Appl. Phys.* **1977**, *48*, 4122−4131.

(70) Cheng, B.; Samulski, E. T. Rapid, High Yield, Solution-Mediated Transformation of Polycrystalline Selenium Powder into Single-Crystal Nanowires. *Chem. Commun.* **2003**, *16*, 2024−2025.

(71) Lu, J.; Xie, Y.; Xu, F.; Zhu, L. Study of the Dissolution Behavior of Selenium and Tellurium in Different Solvents - A Novel Route to Se, Te Tubular Bulk Single Crystals. *J. Mater. Chem.* **2002**, *12*, 2755−2761.

(72) Lu, J.; Xiong, T.; Zhou, W.; Yang, L.; Tang, Z.; Chen, S. Metal Nickel Foam as an Efficient and Stable Electrode for Hydrogen Evolution Reaction in Acidic Electrolyte under Reasonable Overpotentials. *ACS Appl. Mater. Interfaces* **2016**, *8*, 5065−5069.

(73) Voiry, D.; Chhowalla, M.; Gogotsi, Y.; Kotov, N. A.; Li, Y.; Penner, R. M.; Schaak, R. E.; Weiss, P. S. Best Practices for Reporting Electrocatalytic Performance of Nanomaterials. *ACS Nano* **2018**, *12*, 9635−9638.

(74) Zhu, Z.; Yin, H.; He, C.-T.; Al-Mamun, M.; Liu, P.; Jiang, L.; Zhao, Y.; Wang, Y.; Yang, H.-G.; Tang, Z.; et al. Ultrathin Transition Metal Dichalcogenide/3d Metal Hydroxide Hybridized Nanosheets to Enhance Hydrogen Evolution Activity. *Adv. Mater.* **2018**, *30*, 1801171.

(75) Xiong, P.; Zhang, X.; Wan, H.; Wang, S.; Zhao, Y.; Zhang, J.; Zhou, D.; Gao, W.; Ma, R.; Sasaki, T.; Wang, G. Interface Modulation of Two-Dimensional Superlattices for Efficient Overall Water Splitting. *Nano Lett.* **2019**, *19*, 4518−4526.

(76) Subbaraman, R.; Tripkovic, D.; Chang, K.-C.; Strmcnik, D.; Paulikas, A. P.; Hirunsit, P.; Chan, M.; Greeley, J.; Stamenkovic, V.; Markovic, N. M. Trends in Activity for the Water Electrolyser Reactions on 3d M(Ni,Co,Fe,Mn) Hydr(Oxy)Oxide Catalysts. *Nat. Mater.* **2012**, *11*, 550.

(77) Subbaraman, R.; Tripkovic, D.; Strmcnik, D.; Chang, K.-C.; Uchimura, M.; Paulikas, A. P.; Stamenkovic, V.; Markovic, N. M. Enhancing Hydrogen Evolution Activity in Water Splitting by Tailoring Li+-Ni(OH)2-Pt Interfaces. *Science* **2011**, *334*, 1256−1260.

(78) Danilovic, N.; Subbaraman, R.; Strmcnik, D.; Chang, K.-C.; Paulikas, A. P.; Stamenkovic, V. R.; Markovic, N. M. Enhancing the Alkaline Hydrogen Evolution Reaction Activity through the Bifunctionality of Ni(OH)2/Metal Catalysts. *Angew. Chem.* **2012**, *124*, 12663−12666.

(79) Wang, L.; Lin, C.; Huang, D.; Chen, J.; Jiang, L.; Wang, M.; Chi, L.; Shi, L.; Jin, J. Optimizing the Volmer Step by Single-Layer Nickel Hydroxide Nanosheets in Hydrogen Evolution Reaction of Platinum. *ACS Catal.* **2015**, *5*, 3801−3806.

(80) Zhang, J.; Wang, T.; Liu, P.; Liu, S.; Dong, R.; Zhuang, X.; Chen, M.; Feng, X. Engineering Water Dissociation Sites in MoS2 Nanosheets for Accelerated Electrocatalytic Hydrogen Production. *Energy Environ. Sci.* **2016**, *9*, 2789−2793.

(81) Anantharaj, S.; Kundu, S. Do the Evaluation Parameters Reflect Intrinsic Activity of Electrocatalysts in Electrochemical Water Splitting? *ACS Energy Lett.* **2019**, *4*, 1260−1264.

(82) Anantharaj, S.; Ede, S. R.; Karthick, K.; Sam Sankar, S.; Sangeetha, K.; Karthik, P. E.; Kundu, S. Precision and Correctness in the Evaluation of Electrocatalytic Water Splitting: Revisiting Activity Parameters with a Critical Assessment. *Energy Environ. Sci.* **2018**, *11*, 744−771.

(83) Trasatti, S.; Petrii, O. A. Real Surface Area Measurements in Electrochemistry. *J. Electroanal. Chem.* **1992**, *327*, 353−376.

(84) Li, D.; Batchelor-McAuley, C.; Compton, R. G. Some Thoughts about Reporting the Electrocatalytic Performance of Nanomaterials. *Appl. Mater. Today* **2020**, *18*, 100404.

(85) Gopalakrishnan, D.; Lee, A.; Thangavel, N. K.; Reddy Arava, L. M. Facile Synthesis of Electrocatalytically Active NbS2 Nanoflakes for an Enhanced Hydrogen Evolution Reaction (HER). *Sustain. Energy Fuels* **2018**, *2*, 96−102.

(86) Si, J.; Zheng, Q.; Chen, H.; Lei, C.; Suo, Y.; Yang, B.; Zhang, Z.; Li, Z.; Lei, L.; Hou, Y.; Ostrikov, K. (Ken) Scalable Production of Few-Layer Niobium Disulfide Nanosheets via Electrochemical Exfoliation for Energy-Efficient Hydrogen Evolution Reaction. *ACS Appl. Mater. Interfaces* **2019**, *11*, 13205−13213.

(87) Huang, C.; Wang, X.; Wang, D.; Zhao, W.; Bu, K.; Xu, J.; Huang, X.; Bi, Q.; Huang, J.; Huang, F. Atomic-Pillar Effect in PdxNbS2 to Boost Basal-Plane Activity for Stable Hydrogen Evolution. *Chem. Mater.* **2019**, *31*, 4726−4731.

(88) Zhang, M.; He, Y.; Yan, D.; Xu, H.; Wang, A.; Chen, Z.; Wang, S.; Luo, H.; Yan, K. Multifunctional 2H-TaS2 Nanoflakes for Efficient Supercapacitors and Electrocatalytic Evolution of Hydrogen and Oxygen. *Nanoscale* **2019**, *11*, 22255−22260.

(89) Raj, I.; Duan, Y.; Kigen, D.; Yang, W.; Hou, L.; Yang, F.; Li, Y. Catalytically Enhanced Thin and Uniform TaS2 Nanosheets for Hydrogen Evolution Reaction. *Front. Mater. Sci.* **2018**, *12*, 239−246.

(90) Feng, Y.; Gong, S.; Du, E.; Chen, X.; Qi, R.; Yu, K.; Zhu, Z. 3R TaS2 Surpasses the Corresponding 1T and 2H Phases for the Hydrogen Evolution Reaction. *J. Phys. Chem. C* **2018**, *122*, 2382−2390.

(91) Yu, Q.; Luo, Y.; Qiu, S.; Li, Q.; Cai, Z.; Zhang, Z.; Liu, J.; Sun, C.; Liu, B. Tuning the Hydrogen Evolution Performance of Metallic 2D Tantalum Disulfide by Interfacial Engineering. *ACS Nano* **2019**, *13*, 11874−11881.

(92) Li, H.; Tan, Y.; Liu, P.; Guo, C.; Luo, M.; Han, J.; Lin, T.; Huang, F.; Chen, M. Atomic-Sized Pores Enhanced Electrocatalysis of TaS2 Nanosheets for Hydrogen Evolution. *Adv. Mater.* **2016**, *28*, 8945−8949.

(93) Voiry, D.; Salehi, M.; Silva, R.; Fujita, T.; Chen, M.; Asefa, T.; Shenoy, V. B.; Eda, G.; Chhowalla, M. Conducting MoS2 Nanosheets as Catalysts for Hydrogen Evolution Reaction. *Nano Lett.* **2013**, *13*, 6222−6227.

(94) Wang, D.; Wang, X.; Lu, Y.; Song, C.; Pan, J.; Li, C.; Sui, M.; Zhao, W.; Huang, F. Atom-Scale Dispersed Palladium in a Conductive Pd0.1TaS2 Lattice with a Unique Electronic Structure for Efficient Hydrogen Evolution. *J. Mater. Chem. A* **2017**, *5*, 22618−22624.